



HAL
open science

Toward a better comprehension and modeling of hysteresis cycles in the water sorption–desorption process for cement based materials

Harifidy Ranaivomanana, Jérôme Verdier, Alain Sellier, Xavier Bourbon

► **To cite this version:**

Harifidy Ranaivomanana, Jérôme Verdier, Alain Sellier, Xavier Bourbon. Toward a better comprehension and modeling of hysteresis cycles in the water sorption–desorption process for cement based materials. *Cement and Concrete Research*, 2011, 41 (8), pp.817-827. 10.1016/j.cemconres.2011.03.012 . hal-01098091

HAL Id: hal-01098091

<https://hal.science/hal-01098091>

Submitted on 6 Sep 2023

HAL is a multi-disciplinary open access archive for the deposit and dissemination of scientific research documents, whether they are published or not. The documents may come from teaching and research institutions in France or abroad, or from public or private research centers.

L'archive ouverte pluridisciplinaire **HAL**, est destinée au dépôt et à la diffusion de documents scientifiques de niveau recherche, publiés ou non, émanant des établissements d'enseignement et de recherche français ou étrangers, des laboratoires publics ou privés.



Distributed under a Creative Commons Attribution - NonCommercial 4.0 International License

1 **Toward a better comprehension and modeling of hysteresis cycles in the water sorption-**
2 **desorption process for cement based materials**

3 H. Ranaivomanana^{a*}, J. Verdier^a, A. Sellier^a, X. Bourbon^b

4 ^a Université de Toulouse; UPS, INSA; LMDC (Laboratoire Matériaux et Durabilité des
5 Constructions) ; 135, Avenue de Rangueil ; F-31 077 Toulouse Cedex04, France

6 ^b Andra, Parc de la Croix Blanche, 1-7 Rue Jean Monnet, F-92 298 Chatenay Malabry Cedex,
7 France

8 *Corresponding author: hranaivo@insa-toulouse.fr

9 *Abstract: The aim of this work is to describe a method based on a simple representation of the*
10 *pore size distribution, which is able to predict hysteresis phenomena encountered in water*
11 *sorption-desorption isotherms, particularly for cementitious materials. The hysteresis effect*
12 *due to network constrictivity is taken into account in order to extend models of transfer in*
13 *porous media to situations involving wetting-drying cycles. This is not achieved in earlier*
14 *models and their performance in terms of prediction in such conditions is thus limited. The*
15 *present modeling is based on an idealized pore size distribution. This has three modes,*
16 *associated with C-S-H pores, medium capillary pores, and large capillary pores including*
17 *consideration of cracks. The distribution is assessed from the chemical composition of the*
18 *cement, the formulation of the material, the degree of hydration, the total water porosity and*
19 *the intrinsic permeability.*

20 *Keywords: drying, adsorption, cycles, permeability, cementitious materials*

21 **1 State of the art**

22 The modeling of transfer properties through porous media is a widely studied topic, especially
23 in the field of civil engineering with cementitious materials. Pore network models have been
24 developed to assess the liquid and gas permeability [1-6] and the water diffusivity of such
25 materials [7,8], to simulate mercury intrusion [9] or to study the kinetics of capillary

26 imbibition [10]. The aim of our study is to develop a physical model representing the hydric
27 behavior of the porous space. As in previous work, our model is based on the size distribution
28 of pores and can lead to an estimate of the water content of the material, whatever its
29 humidity history. However the proposed study is not restricted to finding the sorption and
30 desorption isotherms but also predicts the non-linear connecting paths anywhere between
31 them. This non-linearity is due to hysteresis.

32 Aligizaki [11] describes the different types of hysteresis (de Boer classification [12] and
33 IUPAC classification [13]) and the different theories on the origin of the hysteresis. The
34 author mentions, among others, McBain [14] and Brunauer et al [15]. Mc Bain explains the
35 hysteresis effect by the presence of ink bottle pores. The wide part is filled at high relative
36 humidity but can only be drained during desorption when the narrow part is at low relative
37 humidity. Brunauer et al. assumed that, for the same pore, capillary condensation and
38 evaporation occurred at different relative humidities. Based on test results of nitrogen
39 adsorption, Aligizaki deduced that the shape of the hysteresis loop obtained on cement pastes
40 was of the B or D type according to the classification of de Boer or the H3 type according to
41 the IUPAC classification. This reflects the fact that the pores are composed of large capillaries
42 with narrow necks or have flattened shapes (corresponding, for example, to the representation
43 of the C-S-H gel structure in sheets). By performing several cycles of wetting-drying at
44 different levels of relative humidity between 3% RH and 100% RH on various cementitious
45 materials, Baroghel Bouny [16-17] infers that hysteresis is present throughout this range of
46 relative humidity. It is significant between 33% RH and 100% RH and the author attributes its
47 origin to the difference between the mechanisms of condensation and evaporation due to the
48 shape of the pores or to the possible presence of different shapes in the liquid-vapor interface.
49 For low RH ($RH < 33\%$), a change of microstructure due to the departure of water strongly
50 bound to the C-S-H explains the hysteresis. Other possible causes cited by the author are the

51 presence of "multi-scale ink-bottle pores" or "kinetic effects" which complicate and delay the
52 establishment of balance especially in the median range of RH where moisture transport is
53 slower due to the discontinuity of the liquid phase. Also according to Baroghel Bouny [16],
54 the hysteresis effect is a short-term phenomenon corresponding to a thermodynamically
55 unstable condition and should subside and disappear after a certain period of time depending
56 on the temperature and relative humidity range. This is confirmed by other researchers, e.g.
57 Ishida et al [18], who suggest a gradual dispersion of water in the ink bottle pores under the
58 effect of temperature. In a recent publication, Poyet [19] uses the heat involved in the
59 adsorption process to explain the effect of temperature on the first desorption isotherm:
60 adsorption is an exothermic process. An increase in temperature hinders the process,
61 decreasing the number of adsorbed molecules and therefore the water content. Conversely, the
62 desorption process is encouraged. Espinosa and Franke [20] explain hysteresis by the fact that
63 the pores affected by capillary condensation are not the same as those affected by desorption
64 for a given relative humidity, when they are accessible at both ends. Capillary condensation
65 takes place without the formation of a meniscus at the liquid-vapor interface (cylindrical). In
66 contrast, menisci appear before desorption takes place. In the case where the pores are
67 accessible only by one end, a meniscus takes form at the liquid-vapor interface in both
68 capillary condensation and desorption. The pore radii involved in both processes are then the
69 same, preventing hysteresis. The authors also associate the hysteresis effect with a
70 modification of the porous structure due to the drying mode (by drying at 105 ° C or freeze-
71 drying), to obtain the dry mass at the end of desorption. The effect of the degree of hydration
72 of the cement, which continues to evolve during the tests, is also mentioned.

73 The models already developed to describe the porous space and simulate moisture transfer in
74 particular for cementitious materials, do not especially include the hysteresis effect. Philippi
75 and Souza [21] propose a 3-scale geometric model of the porous structure of cement and lime

76 mortar in order to study the influence of the model on the simulation of moisture retention and
77 transfer. Bary [22] implements a network model based on pore size distribution to describe
78 moisture transfer in cement-based materials. It is a probabilistic model assimilating porosity
79 to a system of overlapping spheres. With this model, the author connects the degree of
80 saturation with pore size. The relationship obtained is then used with the Kelvin-Laplace law
81 to obtain the isotherm.

82 Generally, when hysteresis is taken into account, the basic principle is always the same. A
83 pore is assumed saturated if its radius is smaller than that obtained by the Kelvin-Laplace.
84 Due to the network constrictivity, this pore is connected to others (with radii larger than that
85 obtained by the Kelvin-Laplace) which remain also saturated. The difference between the
86 proposed approaches lies mainly in the representation of the pore space and therefore the
87 implementation of the model. A probabilistic 2D model of a multi-scale porous network is
88 suggested by Carmeliet et al. [23]. Although their model is able to correctly reproduce the
89 hysteresis, it was developed for materials with a broad pore size distribution composed of
90 only two families. The first was chosen with an equivalent radius equal to or greater than
91 1000 nm and the second with an equivalent radius between 1nm and 1000nm, which is not
92 sufficient to describe cementitious materials. The 3D porous network version of the model is
93 also widely used. It consists of two entities: sites (spherical cavities) interconnected by links
94 (cylindrical pores), each with its own size distribution. Other approaches involve the concept
95 of mathematical morphology (shape description) [24,25]. However, for those models, the list
96 of which is not exhaustive, the relevance to cementitious materials is ignored because they
97 were tested for other types of materials.

98 In the model developed for cementitious materials, Sallee and Quenard [26] address the study
99 of water vapor transfer mechanisms in microporous materials using a hierarchical approach
100 with three levels: microscopic (cylindrical shaped pore), microstructure (simplified

101 representation of the microstructure from network models with a well defined topology) and
102 mesoscopic. The set allows sorption isotherms and vapor permeability to be estimated. In
103 their modeling, the hysteresis effect is taken into account by the fact that a pore can only be
104 desaturated if it has access to a continuous path of air connected to the accessible network.
105 This allows the ink bottle effect, which becomes accentuated when the network is poorly
106 connected, to be integrated. However, besides the fact that the results of the model had not
107 been confronted with experimental results to verify its relevance, it was also tested for only
108 one cycle involving desorption until the dry state was reached. Espinosa and Franke [27] have
109 developed a method to predict the isotherms for cement pastes and mortars. They combine a
110 thermodynamic model of molecular adsorption in porous materials with a cylindrical pore
111 model including ink-bottle pores in order to consider their influence on the hysteresis effect.
112 Ishida, Kishi and Maekawa, [18-28] propose a model of moisture transfer taking the effect of
113 temperature into account. In their modeling, they develop a pore size distribution model
114 (Rayleigh Ritz distribution) able to take account of the hysteresis effect to simulate sorption
115 and desorption isotherms. A residual saturation, noted as S_{ink} , that remains in the pores
116 assumed to be already drained due to the “ink-bottle” effect, is considered on the pore size
117 distribution as shown in Figure 1.

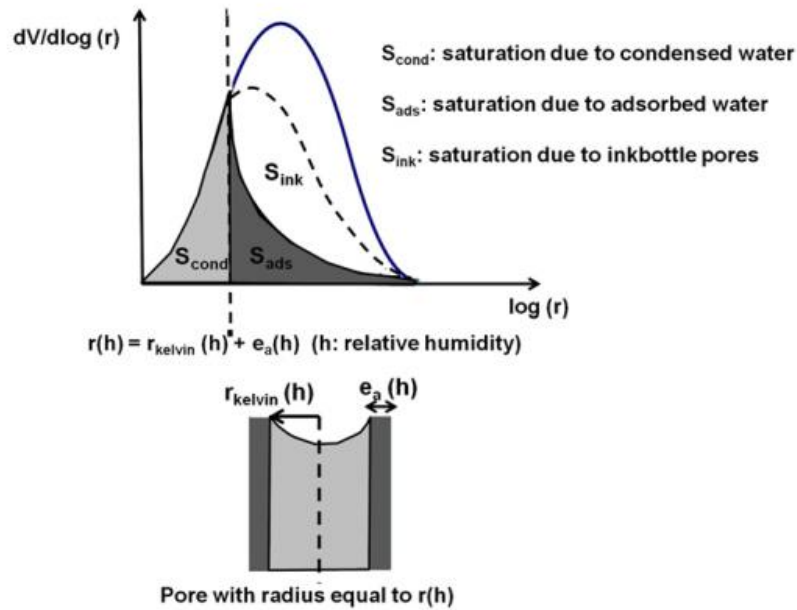


Figure 1: Hysteresis modeling from [18-28]

118

119

120

121 Without questioning the models mentioned above, especially those developed for
 122 cementitious materials, it nevertheless remains true that their performance in predicting
 123 isotherms with particular consideration of the hysteresis effect is uncertain. This is the reason
 124 why we propose some improvements to earlier models, for the management of the hysteresis
 125 cycles. The experimental program implemented to obtain complete data sets is presented first
 126 and the modeling is discussed afterwards.

127 **2 Experimental program**

128 **2.1 Program objectives**

129 The bases of the model proposed in this study were established from the results of isotherm
 130 tests that we carried out for the same reason. Experimental results from the literature were
 131 also used. The materials studied and the main experimental results are described below.

132 **2.2 Materials**

133 The tests were performed on two concretes, denoted C1 and C2, made respectively with
 134 Ordinary Portland Cement (OPC) and Portland Slag Fly ash Cement. These are the concrete
 135 formulations envisioned by Andra for nuclear waste repository structures in deep geologic

136 formations. Isotherms obtained by Hyvert [29] on a OPC-based mortar, denoted M, and the
 137 results obtained by Baroghel Bouny [17] on OPC-based cement pastes (formulations CP1 and
 138 CP2) were also used to evaluate the model. The chemical compositions of the cements used in
 139 each mortar or concrete test specimen are given in Table 1. The formulation of the various
 140 materials and their physical characteristics are in Table 2. For porosity and bulk density
 141 measurements, the samples were saturated under vacuum for at least 24h, then weighted in
 142 water and in air to determine their volume, and dried at 105°C until their mass remains
 143 constant. For the case of cement paste CP2, the bulk density was not measured but estimated
 144 from the amount of hydrates formed by using Eq. (2). The degree of hydration was computed
 145 to 80% by Camps [30] for concrete C1 and 72% for concrete C2. For cement pastes CP1 and
 146 CP2, Baroghel Bouny [17] measured respectively 0.76 and 0.9. Nevertheless, we find that
 147 these values are slightly overestimated. Generally, the cement never reaches a complete
 148 hydration especially in the case of low water/ciment ratio because the accessibility of
 149 anhydrous grains is reduced. According to the formula (Eq.(1)) proposed by Waller [31], the
 150 degrees of hydration are respectively estimated at 68% for cement paste CP1, 77% for
 151 cement paste CP2 and 80% for mortar M.

$$\alpha = 1 - \exp(-3.3 \times \frac{w}{c}) \quad (1)$$

152 Where α is the hydration degree and w/c is the water /cement ratio (kg/kg)

(% by weight)	Test specimens				
	C1	C2	M	CP1	CP2
SiO ₂	20.90	26.88	20.10	22.72	23.44
Al ₂ O ₃	3.20	9.71	4.90	5.16	2.74
Fe ₂ O ₃	4.60	2.91	3.50	2.33	2.50
CaO	65.10	50.74	63.60	64.43	66.20

MgO	0.60	2.73		1.21	0.80
SO ₃	2.76-3.00	2.69	3.50	2.86	2.04
Na ₂ O	0.10	0.20	0.10	0.18	0.43
K ₂ O	0.60	1.06	1.60	0.44	0.43

Table1: Chemical compositions of cements used in each test specimen

153
154
155

	C1	C2	M	CP1	CP2
Cement (kg/m ³)	400.00	450.00	400.00	1502.00	1306.00
Limestone sand 0/4 mm (kg/m ³)	858.00	800.00			
Siliceous sand (kg/m ³)			1212.00		
Limestone gravel 5/12.5 mm (kg/m ³)	945.00	984.00			
Superplasticizer (kg/m ³)	10.00	11.25			
Total water (kg/m ³)	178.00	183.00	200.00	523.00	588.00
Porosity (%)	12.30	14.70	17.20	30.30	40.50
Bulk density (kg/m ³)	2349.00	2291.00	2050.00	1717.00	1500.00
Hydration degree	0.80	0.72	0.80	0.76 (measured) 0.68 (estimated)	0.90 (measured) 0.77 (estimated)

Table 2: Mix design and characteristics of test mixtures

156
157
158
159
160
161

The model proposed in the second part considers a partition of porosity between C-S-H pores and capillary pores. For this, we must determine the amount of C-S-H formed after hydration. Powers and Brownyard [32], make the assumption that the porosity of C-S-H is independent of the degree of hydration and of the water/cement ratio. It is constant and equal to about

162 28%. This intrinsic value of C-S-H porosity was recently highlighted by Baroghel Bouny [16]
 163 from water vapour sorption isotherms. It was also adopted by Maekawa et al. [28] in their
 164 pore structure model of cement paste. The volume of capillary pores occupied by water not
 165 consumed by the hydration is obtained from the difference between the volumes of water and
 166 cement initially present in the paste and the volumes of hydrates formed and of anhydrated
 167 cement. To calculate the volume of C-S-H, we used the approach proposed by Adenot [33]
 168 and adopted by Bary and Sellier [34], using as input the chemical composition of the cement,
 169 the formulation of the material and the degree of hydration (Table 1 and Table 2).
 170 In the case of a material made with OPC, the phases composing the cement matrix are given
 171 in Table 3.

	Chemical formula	Notation
Portlandite	Ca(OH)_2	CH
C-S-H	$1.7\text{CaO} \cdot \text{SiO}_2 \cdot 2.45\text{H}_2\text{O}$	C-S-H
Monosulfate	$3\text{CaO} \cdot \text{Al}_2\text{O}_3 \cdot \text{CaOSO}_3 \cdot 12\text{H}_2\text{O}$	AFm
Ettringite / Hexahydrate	$3\text{CaO} \cdot \text{Al}_2\text{O}_3 \cdot 3\text{CaOSO}_3 \cdot 32\text{H}_2\text{O} /$ $3\text{CaO} \cdot \text{Al}_2\text{O}_3 \cdot 6\text{H}_2\text{O}$	AFt/ C_3AH_6

172 **Table 3 : Hydrates composing the cement matrix**

173
 174 Authors such as Richardson [35] have shown for C-S-H that the average value of the C/S
 175 ratio is around 1.7. This was confirmed recently by Nguyen [36].
 176 The amount of hydrates formed is related to the components of anhydrated cement (CaO,
 177 SiO_2 , Al_2O_3 , SO_3) by the following system of equations

$$\begin{aligned}
 \text{CaO} &= \text{CH} + 1.7\text{CSH} + 4\text{AFm} + 6\text{AFt}(\text{or } 3\text{C}_3\text{AH}_6) & (2) \\
 \text{SiO}_2 &= \text{CSH} \\
 2\text{Al}_2\text{O}_3 &= \text{AFt}(\text{or } 2\text{C}_3\text{AH}_6) + \text{AFm} \\
 \text{SO}_3 &= 3\text{AFt}(\text{or } 0\text{C}_3\text{AH}_6) + \text{AFm}
 \end{aligned}$$

178 This approach is suitable for OPC not for slag or fly ash for instance.

179 The molar volumes of the different phases are given in Table 4 below

	CH	C-S-H	Afm	C ₃ AH ₆
Molar volume (cm ³ /mol)	33.1	88.1	313	150

180 **Table 4: Molar volumes of different phases composing the cement matrix [37]**

181

182 In the case of a material made with cement and additions, which contains slag and fly ash, we
183 have to take into account of the pozzolanic reactions. In fact, the portlandite formed during
184 the hydration of clinker reacts with silica not consumed during the hydration of slag and silica
185 contained in fly ash. The reaction leads to the formation of secondary C-S-H. Their C/S ratio
186 is close to 1 because they occur during the hydration phase, when calcium ions start to
187 disappear from the pore water [28]. We approach the hydration of Portland-Slag-Fly ash-
188 cement by considering first the hydration of clinker, then hydration of slag. The last step is the
189 pozzolanic reaction of fly ash. In our approach, the kinetics of the reactions are not considered
190 but only the quantities of each element which react. These quantities are evaluated from the
191 “mean” value of the hydration degree: 72% which is assessed to correspond to the
192 stabilization of cement hydration. Of course, the approach may be erroneous because it is a
193 simplified view of cement hydration. We assume the porosity of C-S-H formed during the
194 hydration of clinker and the porosity of secondary C-S-H are almost the same, i.e. about 28%.
195 The amount of C-S-H and the distribution of pore volume for 1 m³ of material are given in
196 Table 5. The amount of C-S-H are computed by using Eq. (2). By multiplying the obtained
197 values by the intrinsic porosity of C-S-H (equal to 28%), we obtain the volume of C-S-H
198 pores. Thus, the volume of capillary pores is the remaining percentage required to reach the
199 water porosity.

200

201

Materials	C-S-H amount (m ³)	C-S-H gel pores (m ³)	Capillary pores (m ³)	Porous volume (m ³)
C1	0.098	0.027	0.096	0.123
C2	0.115	0.032	0.115	0.147
M	0.094	0.026	0.146	0.172
CP1	0.353	0.099	0.204	0.303
CP2	0.337	0.094	0.311	0.405

Table 5: Distribution of pore volume for 1m³ of material

In the pore size classification proposed by Mindess et al. [38], the C-S-H gel pores are smaller than 10 nm. Thin capillaries are between 2.5 nm and 50 nm and large capillaries are between 50 nm and 10 µm. The entrapped air bubbles are classified between 100 µm and 1 mm. This pore size classification was adopted for our study. However we did not include entrained air bubbles because they are not totally accessible to water. They are also of little importance in terms of water transfer [11,17].

2.3 Tests

2.3.1 Isotherms

Sorption and desorption isotherms were experimentally obtained from 7 cm × 7 cm × 28 cm prismatic samples. The specimens C1 and C2 were removed from the moulds 24 hours after casting, covered with adhesive foil and stored in endogenous cure conditions in a temperature controlled room at 20°C for one year. At the end of the curing time they were weighted and saturated under vacuum. They were weighted again (immersed and in air) to determine their apparent volume and to obtain their density after the endogenous cure. Then, the specimens were cut in wet conditions into 7 cm × 3.5 cm × 0.5 cm slices that were numbered and coated with resin on their sides. A thickness of 0.5 cm was chosen in order to reach the equilibrium quickly and to limit the test duration. After the setting of the resin (~12h), the slices were then resaturated under vacuum and placed in sealed Plexiglas cells in which the relative humidity

222 was controlled using saturated salt solutions placed in cups. The cells were regularly
223 monitored with a thermo-hygrometer. A small fan ran continuously so as to homogenize the
224 atmosphere in the cells. The cells were placed in a glove box, the role of which was to protect
225 the samples from the atmospheric CO₂ as carbonation modifies the pore network and also the
226 dried mass of the material. This precaution was associated with a regular sweep of nitrogen to
227 remove all the CO₂. The amount of CO₂ remaining in the glove box after 24 hours without
228 sweeping was always below 100 ppm. Specimen masses were monitored during testing using
229 a balance with an accuracy of 1 mg. Equilibrium was reached when the mass of material did
230 not vary by more than 0.01% between two successive weightings. For each level of imposed
231 RH, the weights were measured daily during the first week, then once a week until
232 equilibrium was reached. A mean value extracted from three samples was considered
233 representative of the results, as shown in [16-20]. The different levels of relative humidity
234 with the corresponding saline solutions were: 97% (potassium sulfate), 86% (potassium
235 chloride), 76% (sodium chloride), 55% (dichromate potassium), 44% (potassium carbonate).
236 To highlight the hysteresis effect on different relative humidity levels, four cycles were
237 performed: the first three involved sorption from 76%, 55% and 44% RH after stabilization of
238 the first desorption on the corresponding RH levels, while the fourth was an adsorption from
239 the dry state (Figures 2a to 2e). This dry state is obtained by an oven-drying at respectively
240 50°C, 80°C and 105°C until the mass of samples remains constant. The degree of saturation
241 of a sample is classically given by the relationship:

$$242 \quad S_r = \frac{m - m_0}{m_{sat} - m_0} \quad (3)$$

243 Where m is the mass at equilibrium, m_0 the dried mass, and m_{sat} the saturated mass.
244
245 According to the experimental results (area circled on Figures 2a and 2b), a strong fall in the
246 saturation degree was observed between 100% RH and 97% RH. The fact that the samples

247 had a small thickness (0.5 cm) for a large exposed area (3.5 cm × 7cm) could give the
248 impression that this fall was due to a surface effect. However, the similarity of results with
249 those obtained by Brue [39] for the same materials but on larger samples (cylinders diameter
250 = 3.75 cm, height = 5cm) contradicts this hypothesis. In addition, this effect is noted on other
251 isotherms from the literature found at the same temperature but on different materials [20,29].
252 The drop is also marked on carbonated samples made with different types of cement [29]
253 The fall of the isotherm at high humidity could be associated with a percolating pore network
254 that drained very quickly, as soon as moisture declined. For this reason, we believe that this
255 part of the pore distribution plays an important role in the water permeability of the saturated
256 material. Assumed to be made up of wide capillary pores connected themselves or connected
257 by microcracks, it was modeled by large pores having an average radius related to the
258 intrinsic gas permeability of the material. This is why the capillary pore family was divided
259 into two parts for modeling purposes (as in the Mindess classification). According to the
260 experimental desorption isotherms (Figures 2a to e), it seems that, for CEMI-based materials,
261 the porosity associated with this percolated capillary pores about 25 to 30% of the total open
262 porosity. For the concrete C2, it constitutes about 15% of the total porosity.

263 Between 76 and 97% RH, the degree of saturation of the concrete C2 showed small variations
264 compared to concrete C1. This is quite logical since, in this range of RH, the capillary
265 porosity is affected by water movement [16]. As the concrete C2 contains additives (slag and
266 fly ash), secondary C-S-H are formed by pozzolanic reactions during hydration. The fraction
267 of total porosity associated with capillary pores is therefore reduced. This is not the case for
268 OPC-based concrete. This has been shown recently by Nguyen [36] for blended cements
269 containing silica fume.

270 From a relative humidity close to 50%, the porosity of C-S-H played an important role. The
271 variation in the degree of saturation of the concrete C1 became smaller compared with that of

272 concrete C2. Concerning the intermediate cycles, it was found that the hysteresis effect
 273 became more and more significant as relative humidity from which adsorption starts
 274 decreased. This will be taken into account in the modeling part by an increase of the
 275 connectivity between the fraction of the porous network still filled with water and the fraction
 276 already drained away.

277

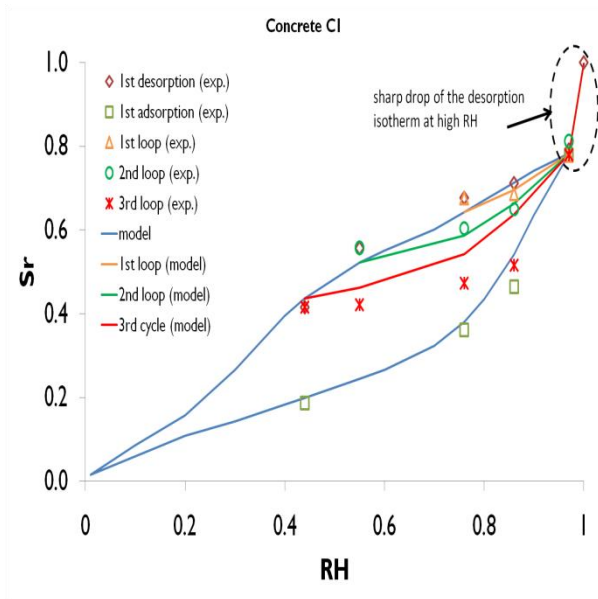


Figure 2a

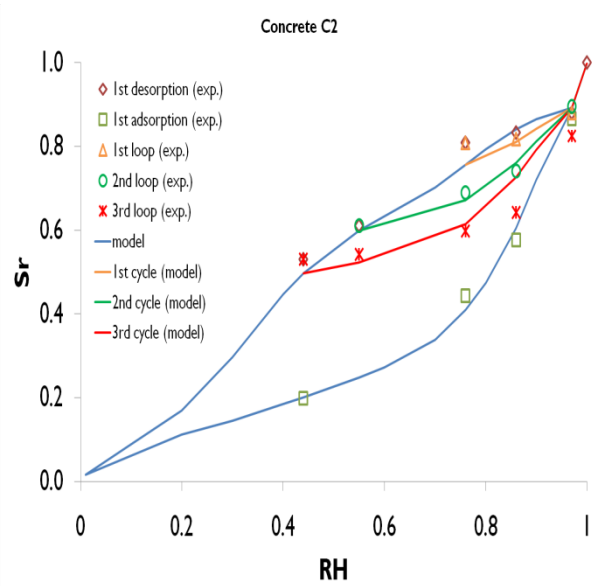


Figure 2b

278
279

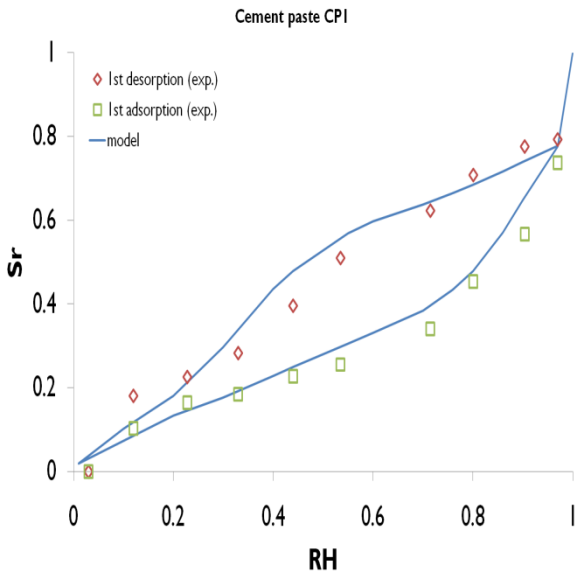


Figure 2c

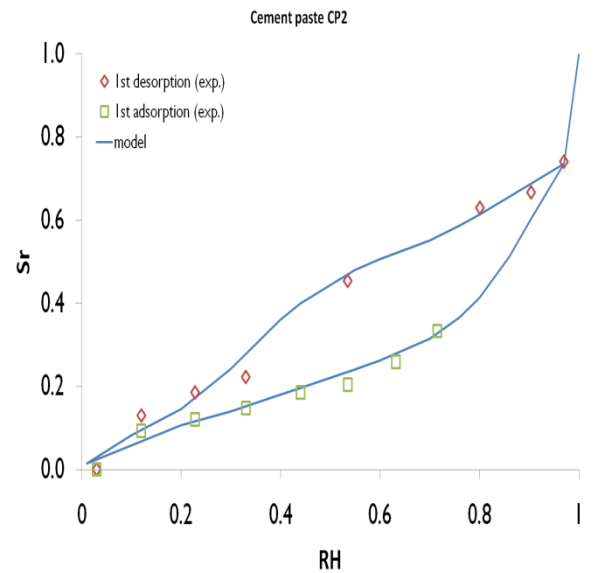


Figure 2d

280
281
282

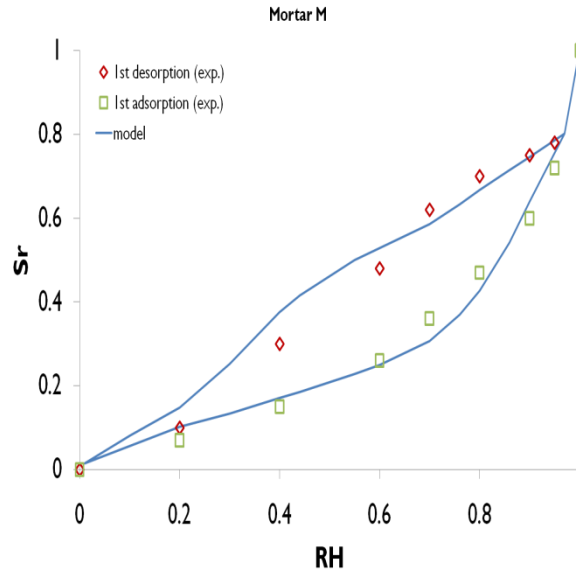


Figure 2e

Figure 2: Experimental results (symbols) and simulated results (solid line)

283
284
285
286

2.3.2 Intrinsic gas permeability

287
288
289
290
291
292
293
294
295
296

Gas permeability was used in this study to obtain the average radius of the large capillary pore family. The intrinsic gas permeability was preferred to water permeability because water has the disadvantage of reacting with the cement paste. It can hydrate the anhydrated cement and also change the chemical equilibria by dissolution, leaching, and/or precipitation of calcite (if the latter is carbonated). Thus, the permeability to water is consistently lower than the permeability measured with gas. Note that ethanol permeability could also have been used since it is of the same order of magnitude as the gas permeability [40]. According to [40], the steady state is reached more quickly when the permeability is measured with ethanol. The values of gas permeability used for the modeling of the porous network are listed in Table 6.

	C1	C2	M	CP1	CP2
K (10^{-17} m^2)	4	5.5	2.5	13	20

Table 6: Values of intrinsic gas permeability

297
298
299
300

The values adopted for concretes C1 and C2 were those obtained by Camps [30] according to the AFPC-AFREM protocol [41]. For mortar M and cement paste CP2, experimental results

301 obtained at LMDC on similar materials with the same protocol were chosen. The gas
302 permeability of CP1 was measured by Baroghel Bouny.[42]

303 **3 Modeling**

304 **3.1 Pore connectivity**

305 The original model, the principle of which was mentioned in paragraph , was developed by
306 Ishida et al. [18]. On the same basis, the hysteresis effect was represented by the
307 implementation of a pore size distribution in which the pores supposed to be drained at a
308 given RH were taken to be only partially drained. Assuming that drying occurs by vapor
309 diffusion in the unsaturated network, pore drying is then possible when the pore is directly
310 connected to the dry network. As the dried space increases when the RH decreases, the
311 probability of connection of a saturated pore to the dry network increases with drying. This
312 explains the decrease of hysteresis in the range of low relative humidity. First, let us consider
313 that pores are cylindrical. Assuming that drying affects pores size r_1 when the relative
314 humidity is h_1 , the drained portion of the porous network represents a fraction of pores of
315 radius larger than r_1 . This fraction depends on the connectivity between the drained portion
316 and pores of radius r_1 . It is very likely that, the longer the developed length of pores with
317 radius bigger than r_1 , the greater their potential connectivity. In fact, most of these pores are
318 long, so they are able to intercept pores of various sizes. The length of a pore is a concept
319 difficult to handle. Valckenborg et al. [43] have determined pore size distribution of a mortar
320 by NMR which measures the true pore volume-to-surface area ratio. They highlighted a
321 bimodal distribution with a first peak at 20nm corresponding to capillary pores and a second
322 peak close to 5nm corresponding to C-S-H pores. The pore size distribution obtained by the
323 authors shows that the pore volume fraction associated to the C-S-H pores is greater than the
324 one associated to the capillary pores. This was confirmed by the pore size distribution
325 determined by other techniques like water vapor adsorption. These results seem to agree with

326 the fact that small pores are long. For this reason, we assume that the probability of
 327 interconnection of pores with radius greater than r_1 can be approximated by the ratio between
 328 the total length of pores which $r > r_1$ to the cumulative total length of all pores of the network
 329 considered (Eq. (4)).

$$P_c(r > r_1) \approx \frac{\int_{r_1}^{r_{\max}} \frac{1}{a(r)} \frac{dV}{d \log r} d \log r}{\int_{r_{\min}}^{r_{\max}} \frac{1}{a(r)} \frac{dV}{d \log r} d \log r} \quad (4)$$

330 Where $a(r)$ is the pore sectional area defined by Eq. (7). $dV/d \log r$ is the density function of
 331 the pore size distribution, (approximated by Eq. (21) in the model).

332 We will see in the paragraph 3.4 that the pore size distribution involved in our model has 3
 333 modes which are respectively associated to C-S-H pores, thin capillary pores and large
 334 capillary pores. These large capillary pores are assumed to be microcracks which are
 335 connected to themselves and are responsible for the sharp drop of the desorption isotherm at
 336 high RH as mentioned earlier. Thus for these pores, we can write that $P_c(r > r_1)$ is equal to 1.

337 Eq. (4) is so only valid for C-S-H pores and thin capillary pores. We then propose to
 338 normalize the function P_c by taking into account the porosities corresponding to each mode.

339 The normalized function is noted as P_c^* and is given by Eq. (22)

340 In Eq. (5), the term under the integral represents the length associated with the elementary
 341 class of pore with radius r .

$$dl = \frac{1}{a(r)} \frac{dV}{d \log r} d \log r \quad (5)$$

342 If we assume a constant pore volume, the smaller the pore cross-sectional area $a(r)$, the longer
 343 the pore. If all pores have cylindrical shapes, the thinnest would have great developed lengths.

344 Of course, they would be able to connect the larger pores and they could lead to considerable
 345 hysteresis even at low relative humidity. C-S-H have been characterized as nodules of

346 $60 \times 30 \times 5 \text{ nm}^3$ [44]. Due its layered structure [44,45], there is no reason to consider cylinders
 347 for the fine pores inter-nodules. This leads us to propose a flattened shape for pores with
 348 lower radii, approximated by an oblong geometry (Figure 3).

349

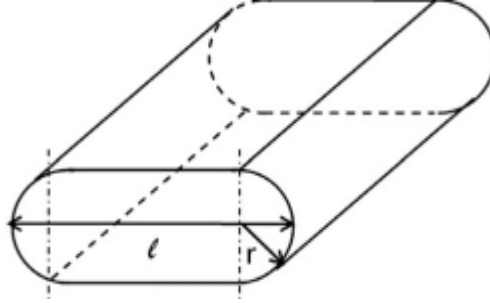


Figure 3: Oblong shaped pore

350

351

352

353

354

355 This kind of pore will be seen by mercury intrusion porosimetry (MIP) or water vapor
 356 adsorption as a pore of radius r . This form can be characterized by an aspect ratio A_p , defined
 357 as the ratio between the width and the height of the pore section. For the reasons mentioned
 358 above, the coefficient A_p evolves to flatten the pores with small radius. An exponential law is
 359 proposed to model this (Eq. (6)).

$$A_p(r) = \frac{l}{2r} = \max\left(\exp\frac{r_{cr}}{r}; 1\right) \quad (6)$$

360 Where r_{cr} is a calibration parameter called the “critical radius”. This parameter can also be
 361 interpreted as the radius below which pores feature a more oblong than cylindrical shape, and
 362 could be the threshold between capillary and C-S-H pores.

363 According to this function, the large pores are cylindrical, as their aspect ratio cannot exceed
 364 1, and the pores become progressively flattened as r decreases.

365 The cross-sectional area of the pore is

$$a(r) = (4(A_p(r) - 1) + \pi)r^2 \quad (7)$$

366 **3.2 Adsorption and capillary condensation**

367 At relative humidity h , the pore radius subjected to condensation is given by the relationship:

$$r(h) = r_k(h) + e_a(h) \quad (8)$$

368 Where $r_k(h)$ and $e_a(h)$ respectively denote the capillary condensate radius and the thickness of
 369 adsorbed water on pore walls.

370 In the case of a cylindrical pore, the capillary condensation radius is given by the Kelvin-
 371 Laplace equation

$$r_{kl}(h) = -\frac{2\sigma M_v}{\rho RT \ln(h)} \quad (9)$$

372 Where

373 σ (N/m) is water / vapor interfacial tension, M_v (kg/mol) the molecular mass of water , ρ
 374 (kg/m³) the water density, R (8.32 J/kg/mol) the ideal gas constant and T (K), the absolute
 375 temperature.

376 It is well known that the interfacial tension depends on the ionic concentrations of the pore
 377 solution which can also modify equilibrium of the liquid-vapor interface and consequently the
 378 Kelvin relation. This fact was studied for example by Monlouis Bonnaire [46]. We decide to
 379 keep the initial relation of Kelvin (Eq.9) and to neglect these effects for sake of simplification.
 380 For this study, the interfacial tension is only a function of the temperature.

$$\sigma(T) = (128 - 0.185T) \times 10^{-3} \quad (10)$$

381 A relation adopted by Maekawa et al. [28] is used for the dependence of water density with
 382 temperature

$$\rho(T) = 1.54 \times 10^{-8} T^3 - 1.85 \times 10^{-5} T^2 + 6.65 \times 10^{-3} T + 2.47 \times 10^{-1} \quad (11)$$

(273K < T < 373K)

383 It is clear that Eq. (9) is no longer valid when the pore features a higher surface/volume ratio.
 384 When the flattening progresses, the pores are comparable to oblong prisms. The relationship
 385 of Kelvin-Laplace tends towards marked flattening

$$r_{k2}(h) = -\frac{\sigma M_v}{\rho RT \ln(h)} \quad (12)$$

386 The transition from Eq. (9)-(12) is ensured by (13)

$$r_k(h) = -\frac{(1 + \alpha)\sigma M_v}{\rho RT \ln(h)} \quad (13)$$

387 The term α is a function of the aspect ratio $A_p(r_{kl})$, $\alpha=1$ when $A_p(r_{kl}) = 1$ and 0 when A_p
 388 $(r_{kl}) = A_{pmax}$. A value of 4 was adopted for A_{pmax} . This allowed us to limit transition from
 389 Eqs (9)-(12) (corresponding to the passage of α from 1 to 0) to a small range of pore sizes, in
 390 order to be able to neglect the effect of the transition on the isotherm shape without causing
 391 singularities during the numerical implementation of the model. It is likely that the oblong
 392 shape becomes dominant from an aspect ratio around this value. Moreover whatever the value
 393 in this order of magnitude, there is no effect of the value on the results. The expression for α
 394 is given by Eq. (14)

$$\alpha = \max\left[1 - \left(\frac{A_p(r_{kl}) - 1}{3}\right); 0\right] \quad (14)$$

395 In Eq. (14), we choose in first order a linear assumption. This is a simplifying hypothesis.
 396 For the expression of $e_a(h)$ used in Eq. (8), the BET model was used [47]. This gives the
 397 number of adsorbed water molecule layers n as a function of the relative humidity h and
 398 temperature T

$$n = \frac{Ch}{(1-h)[1+(C-1)h]} \quad (15)$$

399 C is the BET constant depending on temperature

$$C = \exp\left[\frac{E_1 - E_l}{RT}\right] \quad (16)$$

400 Where E_1 (J/mol) is the molar energy of adsorption of the first layer and E_l (J/mol), the molar
 401 energy of liquefaction of the adsorbate.

402 C depends on the adsorbate / adsorbent pair. However, for the purposes of this model, we
403 adopted the expression used by Xi et al. [48].

$$C = \exp\left(\frac{855}{RT}\right) \quad (17)$$

404 $e_a(h)$ is then obtained by multiplying n by a water molecule size ($\sim 3.10^{-10}$ m)

$$e_a(h) = 3 \times 10^{-10} \times n(h) \quad (18)$$

405 **3.3 Hysteresis**

406 If the humidity decreases from h_1 to $h_2 < h_1$, then the pores with radii between $r_1=r(h_1)$ and
407 $r_2=r(h_2)$ are partially drained. The residual degree of saturation of pores with radii greater than
408 r_2 , noted as S_{ink} , is in the context of the present model, dependent on their connectivity to the
409 dry network. This connectivity is in turn dependent on the probability of interconnection of
410 pores with sizes are greater than r_2 . Therefore, we propose to adopt the following relationship
411 as a first approximation.

$$S_{ink} = 1 - P_c^*(r > r_2) \quad (19)$$

412 If the relative humidity increases from h_1 to $h_3 > h_1$ (corresponding to a pore radius r_3), the
413 pores with sizes between r_1 and r_3 belonging to the dry portion of the network are instantly
414 saturated again. Of course, the volume of water present in pores with radius greater than r_3 but
415 drained only via smaller pores, remains constant.

416 By noting S_r , the degree of saturation of a pore with radius r and \dot{h} the rate of change of
417 relative humidity during the time dt , the mechanisms can be summarized as follows.

$$\begin{aligned}
& \text{If } h \geq 0 \text{ then} \\
& S_r = 1 \quad \forall r \leq r(h + h dt) \\
& S_r = 0 \quad \forall r > r(h + h dt) \\
& \text{If } h < 0 \text{ then} \\
& S_r = 1 \quad \forall r \leq r(h + h dt) \\
& S_r(t + dt) = \min(S_{ink}, S_r(t)) \quad \forall r > r(h + h dt)
\end{aligned}
\tag{20}$$

418 Eq. (20) is the equation key.

419 **3.4 Numerical implementation**

420 It is clear that the management of saturation increments based on relative humidity increments
421 can be treated easily only on a numerically discretized porous network. To this aim, the pore
422 size distribution was discretized and the probability of inter-connectivity (eq 4) was also
423 approximated by a linear interpolation from one discrete radius to another. This is a
424 simplifying hypothesis.

425 As explained earlier, it is necessary to consider several modes, respectively associated with
426 the C-S-H gel pores, the thin capillary pores and the large capillary pores. From an analytical
427 point of view, polynomials of degree 2 of $\log(r)$ are juxtaposed to represent the distribution.
428 In fact, these polynomials are easily differentiable analytically. Thus, a mode can be
429 represented by four portions of parabola. Each parabola is defined by a range of $\log(r)$ with a
430 width equal to δ and a height equal to $H/2$ on the axis $dV/d\log(r)$ (Figure 4).

431

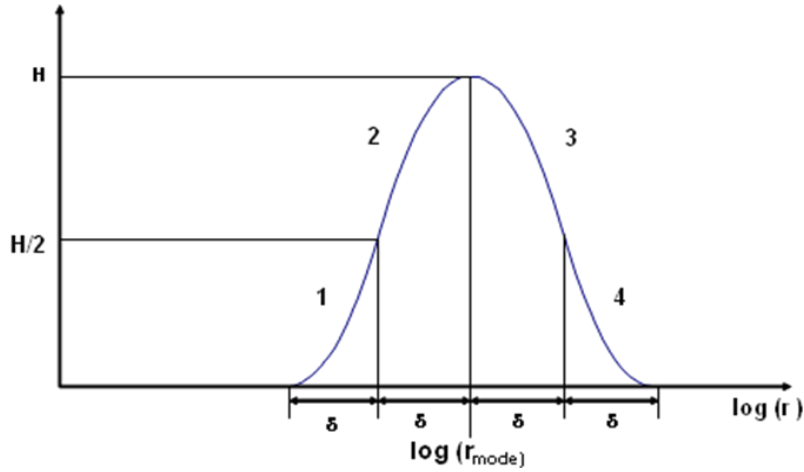


Figure 4: Mode representation with four portions of parabola

432
433
434
435

436 For a distribution containing 3 modes

$$\frac{dV}{d \log r} = \bigcup_{i=1}^{i=3} \left(\bigcup_{j=1}^{j=4} (\beta_{ji}^1 (\log r)^2 + \beta_{ji}^2 (\log r) + \beta_{ji}^3) \right) \quad (21)$$

437 Where the coefficients β_{ji}^k ($k=1$ to 3) depend on three parameters: the modal radius $r_{mode\ i}$, the
438 amplitude, δ , and the height H_i .

439 This simplified representation with three modes allows pore volumes to be calculated
440 analytically and the number of parameters describing the distribution to be limited. Once
441 defined, the modes are discretized as shown in Figure 4. Beyond 100 discretizations, the
442 number of discretizations has no effect on the simulation results. The model was implemented
443 using the free software SCILAB [49].

444 **3.5 Model calibration**

445 **3.5.1 Calibration of modes associated with C-S-H gel pores and thin capillary pores**

446 The pore size distribution used in this model is assumed to be the "real" distribution, not the
447 one obtained from mercury intrusion tests, which is an image of the real distribution. It
448 provides only the access radius into a given pore volume. Because of the "ink-bottle effect",
449 this volume may contain large pores that are accessible through smaller ones. Furthermore,
450 the characterization of pore structure by mercury intrusion tests is limited because the finest

451 pores are not accessible due to limitations of the apparatus (access radius limited to around
452 3nm).

453 To comply with the classification proposed by Mindess et al. [38] (see paragraph 2) the
454 following values were imposed: $\delta = 0.4$ associated with a value of r_{mode} fixed at 1.5 nm for the
455 first mode (r_{C-S-H}) and 9.5 nm for the second mode (r_{thin}). In order to limit the number of
456 fitting parameters, a single value of δ was used for the three modes. As discussed in the next
457 section, the value of intrinsic permeability allows the determination of the radius of the mode
458 associated with large connected capillaries (r_{large}). It is assumed that these capillaries play a
459 major role in the permeability; this stage is explained in the following section. Finally, the
460 height h depends directly on the porosity associated with each mode. The porosity was
461 designated by ϕ_1 for the C-S-H, by ϕ_2 for the small capillaries, by ϕ_3 for large capillaries.
462 These porosities are defined in relation to the total volume of the material. The normalized
463 probability of interconnection P_c^* is then defined by Eq.(22).

$$\begin{aligned} & \text{If } \log r > \log(r_{large}) - 2 \times \delta \text{ then} \\ & P_c^*(r > r_1) = 1 \\ & \text{Else } \log r < \log(r_{large}) - 2 \times \delta \text{ then} \\ & P_c^*(r > r_1) = \frac{1}{\phi} [(\phi - \phi_3) \times P_c(r > r_1) + \phi_3 \times 1] \end{aligned} \tag{22}$$

464 3.5.2 **Calibration of the third mode associated with large capillary pores**

465 Considering that large capillaries are primarily responsible for the water permeability of
466 saturated material, r_{large} was calibrated according to the intrinsic permeability using a classical
467 permeability model..

468 Many authors have used the Katz-Thompson relation to determine the liquid permeability
469 through the distribution of pore size obtained by mercury porosimetry [50-52]. Other
470 approaches based on an analytical method [53] or on a pore network model [1,2] have also
471 been developed. However, they involve the results of mercury porosimetry associated with

472 some empirical considerations. Therefore they were not used as part of our model. The simple
473 capillary model developed by Dullien [54] quoted in [55] was adopted. This model consists of
474 calculating the permeability K with a cylindrical pore model involving Poiseuille's law and
475 Darcy's law.

476 The volume flow q (m^3/s) through a cylindrical pore of radius r (m) is related to the pressure
477 gradient $\Delta p/l$ by Poiseuille's law

$$q = \frac{\pi r^4}{8\mu} \frac{\Delta p}{l} \quad (23)$$

478 Where μ (Pa.s) is the viscosity of fluid through the pore

479 The volume flow Q (m^3/s) through the material is given by Darcy's law

$$Q = \frac{K}{\mu} A \frac{\Delta p}{l} \quad (24)$$

480 Where A (m^2) is the material cross-sectional area.

481 The permeability, K , is obtained by setting the volume flow through the material equal to the
482 sum of flows through the pores.

483 By integrating the tortuosity T , the relationship between the permeability, K , on the one hand
484 and the mode radius r_{large} and porosity ϕ_3 on the other becomes:

$$K = \frac{\phi_3 r_{\text{large}}^2}{8T^2} \quad (25)$$

485 The porosity ϕ_{large} is estimated from the drop of the desorption isotherm at high RH, which is
486 associated to large capillaries connected themselves or connected to microcracks.

487 From Eq (25), we obtain r_{large} (m)

$$r_{\text{large}} = 2T \sqrt{\frac{2K}{\phi_3}} \quad (26)$$

488 Generally, the tortuosity T is related empirically to the porosity. A relationship attributed to
489 Carniglia [56] is for example used by Aït Mokhtar et al. [2]. Other expressions found by other

490 authors are related by Matyka et al. [57]. Among those proposed, we kept the relation
 491 developed by Comiti and Renaud [58] to calculate the tortuosity for fixed beds of
 492 parallelepipeds with different thickness-to-side ratios.

$$T(\phi_{large}) = 1 - 0.86 \ln(\phi_{large}) \quad (27)$$

493 3.5.3 Calibration of critical radius r_{cr}

494 The critical radius r_{cr} , defining the transition value between cylindrical and oblong pores was
 495 set to 1.6 nm, which is common for all the materials studied. This value was obtained after an
 496 inverse analysis. It corresponds to a Kelvin radius for 47 % RH at $T = 20^\circ \text{C}$. Our approach is
 497 in agreement with Nguyen [36]. The author distinguishes two distinct areas: one for low
 498 values of RH, where the amount of hydrates plays a dominant role in water movement, and a
 499 second for high values of RH, where porosity is the most important parameter. These two
 500 areas are separated by an RH threshold value of around 44%. In the proposed model, this
 501 radius also corresponds to r_{cr} , which is precisely the transition radius between cylindrical and
 502 oblong pores.

503 All the data used in the model for each material tested are summarized in Table 7

	Porosity (%)	r_{C-S-H} (nm)	ϕ_1 (%)	r_{thin} (nm)	ϕ_2 (%)	r_{large} (nm)	ϕ_3 (%)	δ	r_{cr} (nm)
C1	12.300	1.5	2.700	9.5	6.520	410	3.080	0.4	1.6
C2	14.700		3.200		9.300	580	2.200		
M	17.200		3.280		10.100	225	3.800		
CP1	30.300		9.600		13.700	385	7.000		
CP2	40.500		9.230		16.920	350	11.340		

Table 7: Data used for each material tested

504
 505
 506 Figure 5 (5a to 5e) highlights the corresponding pore size distributions

507
508

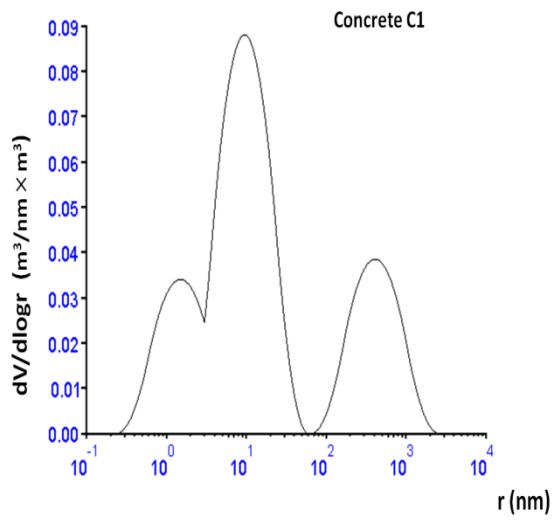


Figure 5a

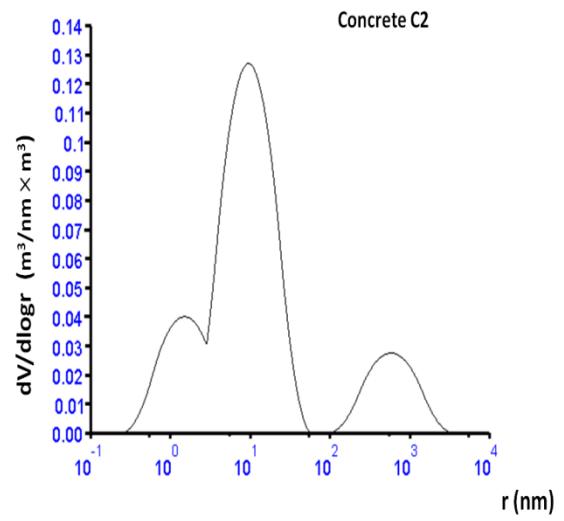


Figure 5b

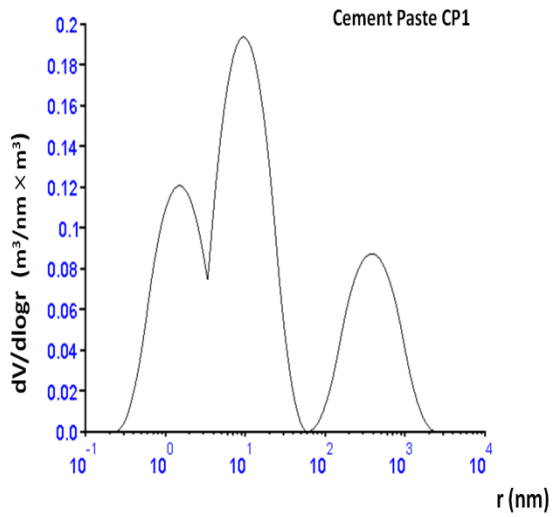


Figure 5c

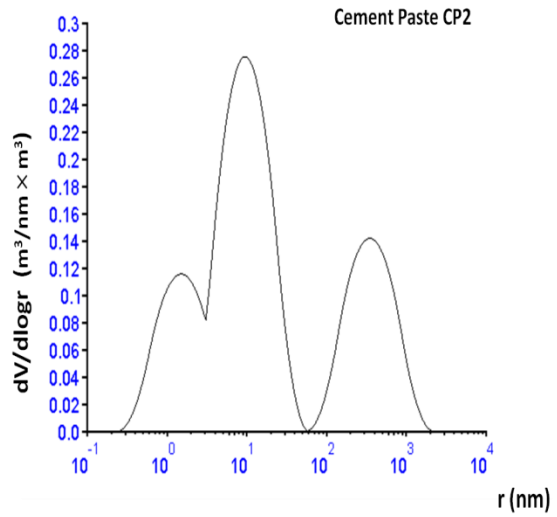


Figure 5d

509
510

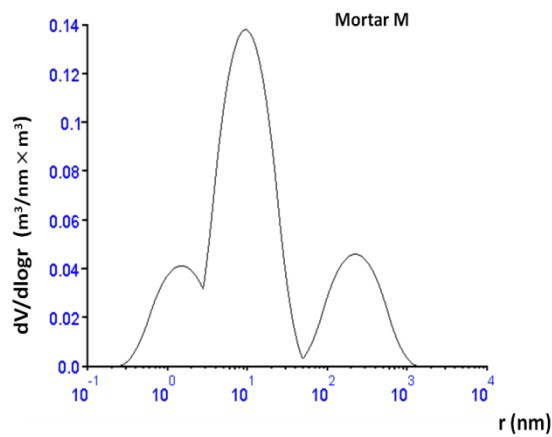


Figure 5e

Figure 5: Proposed pore size distribution for the materials studied

511
512
513

514 **4 Results and comments**

515 The idealized pore size distribution involved in this study is assessed from parameters which
516 are easily measurable or computable: the degree of hydration, the porosity accessible to water
517 and the intrinsic gas permeability. The other necessary data are the chemical composition of
518 the cement and the formulation of the material. The distribution is represented by elementary
519 functions: polynomials of degree 2. The modal radius values are fixed except that of the
520 mode associated to the coarse pores calibrated from gas permeability. The amplitude of each
521 mode is also fixed. The model is then easy to implement. In the function describing the
522 connectivity of the porous network, which essentially makes the originality of this work, the
523 only residual calibration parameter is the critical radius which corresponds to the transition
524 between cylindrical shape associated to capillary pores and oblong shape associated to C-S-H
525 pores. This value is the same for all the materials studied: 1.6 nm. As seen in Figures 2a to e,
526 the model realistically reproduces first desorption and first adsorption isotherms and
527 especially the hysteresis loops.

528 The model can also estimate the specific surface S_s by multiplying pore perimeters by their
529 lengths and summing the results obtained. The theoretical surface can be compared with
530 experimental results.

	S_s model (m^2/g)	S_s exp. (m^2/g)
C1	16.2	20-25 (BET)
C2	21.2	
M	21.4	-
CP1	66.2	83 (BET)
CP2	80.2	123 (BET)

531 **Table 8: Comparison between specific surfaces calculated from the model and experimental specific surfaces**

532
533 Baroghel Bouny [17] has made measurements of specific surface by the BET method on an
534 ordinary concrete and high-performance concrete. The BET method aims to quantify the
535 surface accessible to molecules of gas in the pores of a material. The values obtained by the
536 author, with water vapor as adsorbate, are around 20 to 25m²/g. They are even of the same
537 order of magnitude as the values provided by the model for concretes C1 and C2. For cement
538 pastes CP1 and CP2, the model also gives values of the same magnitude as those measured.
539 For comparison, the pore size distributions obtained by mercury intrusion for concretes C1
540 and C2 are given in Figure 6. For concrete C1, we can distinguish one mode with an access
541 radius around 50 nm (Figure 6a). For concrete C2, we have 2 modes whose access radii are
542 respectively 20 and 1000 nm (Figure 6b). It is likely that the second mode is an artifact
543 because the results obtained by Brue [39] on a similar material don't reveal its presence.
544 The comparison between the theoretical porosity distribution used in the model (1) with that
545 obtained by mercury intrusion (2) for concretes C1 and C2 are given in Figure 7. In our case,
546 the mercury porosity gives access only to pores (assumed cylindrical) with radii above 3.8 nm
547 (Figure 7a and 7b).

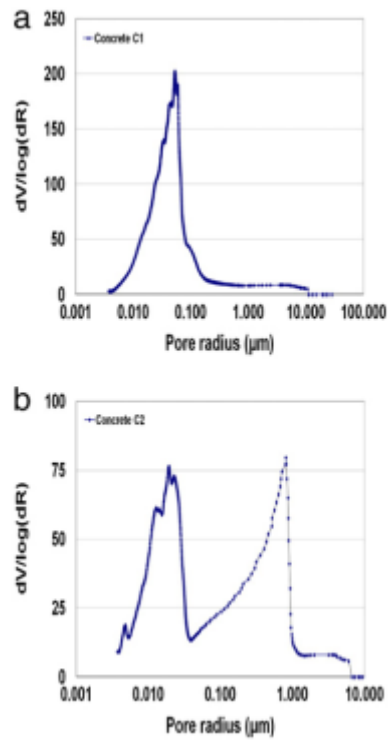


Figure 6: MIP results for concretes C1 and C2

548

549

550

551

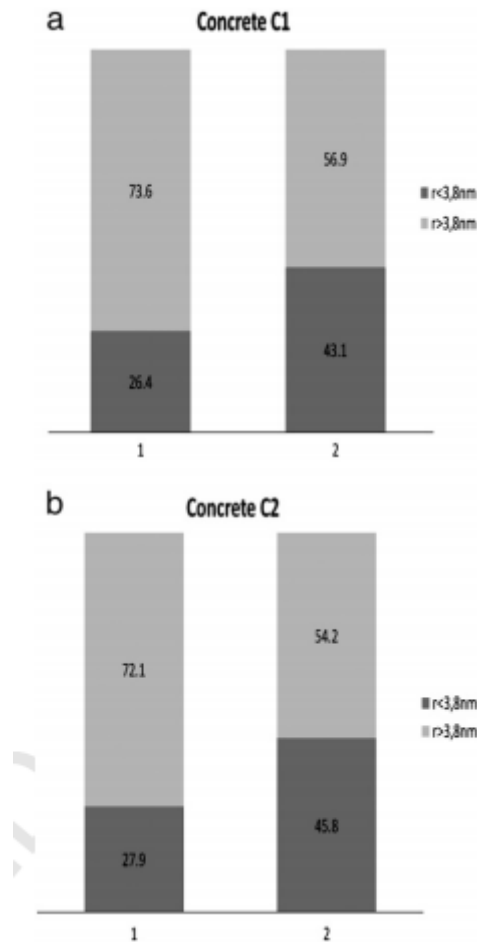


Figure 7: Theoretical porosity distribution (1) and distribution obtained by mercury intrusion (2)

It is not surprising that the mercury porosimetry significantly overestimates the volume of small pores, because of the ink bottle effect. Figure 7 shows that great quantities of large pores are accessible only through smaller pores. The fineness of the cement used for concrete C2 is also highlighted (proportion of finest pores is greater for C2).

5 Conclusions

A physical porous network model has been developed for cement-based materials, to simulate the water sorption-desorption isotherms and to predict any hysteresis. Modeling is based on a trimodal pore size distribution. The modes are associated with C-S-H pores, thin capillaries, and large capillaries connected themselves or connected by microcracks. It is assumed that the large capillaries form a percolating network responsible for the sharp drop in the saturation degree at high relative humidity in the desorption isotherm. Therefore, they play an essential

566 role in the water permeability of the saturated material. Each mode is characterized by 3
567 parameters: the mode radius, r_{mode} , the amplitude, δ , and the height, H . The value of δ is fixed
568 at 0.4 (in $\log(r)$, with r in nm) with a value of r_{mode} equal to 1.5 nm for the first mode $r_{\text{C-S-H}}$ and
569 equal to 9.5 nm for the second mode r_{thin} . For the third mode, r_{large} , the value is calculated
570 from the intrinsic gas permeability. The ethanol permeability can also be used. The height, H
571 is computed from the porosity associated with each mode. The distribution of pore volume
572 between different modes is obtained by calculating the amount of C-S-H formed which
573 constitute the first mode and by using the initial drop in the desorption isotherm to estimate
574 large capillaries. The porosity associated with the central mode is the remaining percentage
575 required to reach the total porosity. The other data used in the model are deduced from the
576 chemical composition of cement, the formulation of the material, the degree of hydration and
577 the open porosity (measured with water as the wetting liquid).

578 To manage the hysteresis, a function of inter-connectivity is associated with the pore size
579 distribution. This function is then used to calculate the residual saturation due to the ink-bottle
580 effect, assuming that pore drying is only possible if the pore is directly connected to a dry
581 network. The inter-connectivity is approximated by the ratio between the total length of pores
582 affected by drying for a given relative humidity and the total cumulative length of all pores of
583 the network. An oblong geometry is attributed to small pores with a progressive dimensions
584 ratio managed by an aspect ratio involving a parameter noted r_{cr} (critical radius). The value of
585 this parameter, obtained by inverse analysis, is set to 1.6 nm, a common value for all the
586 materials studied. This value corresponds to the transition size between cylindrical pores and
587 oblong pores.

588 The conditions for changing the degree of saturation are then numerically managed on a
589 discretized network.

590 The simulations were performed on one concrete, one mortar and two cement pastes made
591 with OPC and on a concrete made with Portland-slag-fly ash-cement. The results obtained
592 show that, with only one fitting parameter (r_{cr}) common to all the material, the model
593 adequately restitutes the experimental results, in particular the hysteresis loops. On the other
594 hand, the values of specific surface area calculated using the model are of the same order of
595 magnitude as those measured experimentally by the BET method.

596 The next step is to extend the model to predict isotherms (i) on leached or carbonated
597 materials by changing the pore size distribution and (ii) at high temperature (taking into
598 account the dependence of the connectivity with temperature). The prediction of water
599 sorption isotherms on early aged materials by the model is also an interesting perspective to
600 this study. For this purpose, an evolution law of the degree of hydration could be proposed . in
601 this case, an adjustment of the parameters which define each mode on the pore size
602 distribution is of course necessary.

603 **6 Acknowledgements**

604 We wish to express our thanks to Andra (French National Agency for Radioactive Waste
605 Management) for its scientific and financial support to the project that led to the development
606 of this model.

607 **7 References**

608 [1]: D Breysse , B Gerard, Modelling of permeability of cement based materials, Part I:
609 Uncracked medium, Cement and Concrete Research, vol. 27, n°5, 1997, pp 761-775.

610 [2]: A Aït-Mokhtar , O Amiri , P Dumargue P, S Sammartino , A new model to calculate
611 water permeability of cement based materials from MIP results, Advances in cement research,
612 vol. 14, n°2, 2002, pp 43-49.

613 [3]: O Amiri, A Aït-Mokhtar, M Sarhani, Tri-dimensional modelling of cementitious
614 materials permeability from polymodal pore size distribution obtained by mercury intrusion
615 porosimetry test, *Advances in cement research*, vol. 17, n°1, 2005, pp 39-45.

616 [4]: G Ye, P Lura, K van Breugel , Modelling of water permeability in cementitious materials,
617 *Materials and Structure*, vol.39, n°9, 2006, pp 877-885

618 [5]: H W Song, SJ Kwon , Permeability characteristics of carbonated concrete considering
619 capillary pore structure, *Cement and Concrete Research*, vol. 37, n°6, 2007, pp 909-915.

620 [6]: JP Monlouis Bonnaire, J Verdier, B Perrin, Prediction of the relative permeability to gas
621 flow of cement based materials, *Cement and Concrete Research*, vol. 34, n°5, 2004, pp 737-
622 744.

623 [7]: B Pradhan, M Nagesh, B Bhattacharjee, Prediction of the hydraulic diffusivity from pore
624 size distribution of concrete, *Cement and Concrete Research*, vol. 35, n°9, 2005, pp 1724-
625 1733.

626 [8]: S Bejaoui, B Bary, Modeling of the link between microstructure and effective diffusivity
627 of cement pastes using a simplified composite model, *Cement and Concrete Research*, vol.
628 37, n°3, 2007, pp 469-480.

629 [9]: R Vöckel, C Gallé, M Dubois, P Lovera, Mercury intrusion porosimetry and hierarchical
630 structure of cement pastes, *Cement and Concrete Research*, vol. 30, n°4, 2000, pp 521-527.

631 [10]: A Laventis, D A Verganelakis, M R Halse, J B Webber, J H Strange , Capillary
632 imbibition and pore characterisation in cement pastes, *Transport in porous media*, vol.39, n°2,
633 2000, pp 143-157.

634 [11]: K Aligizaki, Pore structure of cement based materials: testing, interpretation and
635 requirements, *Modern Concrete Technology* 12, Spon Press, 2006.

636 [12] : J H de Boer, "The shapes of capillaries" in The Structure and Properties of Porous
637 Materials, in Proceedings of the Tenth Symposium, Colston Research Society University of
638 Bristol, Everett D.H, Stone F.S, Butterworths Science Publications, London, 1958, pp 68-94.

639 [13]: K S W Sing, D H Everett, R A W Haul, L Moscou, R A Pierotti, J Rouquérol, T
640 Siemieniewska, Reporting physisorption data for gas/solid systems with special reference to
641 the determination of surface area and porosity, Pure and Applied Chemistry, vol.57, n°4,
642 1985, pp 603-619.

643 [14]: J W Mc Bain, An explanation of hysteresis in the hydration and dehydration of gels,
644 Journal of the American Chemical Society, Vol.57, n°4, 1935, pp 699-700.

645 [15]: S Brunauer, R Sh Mikhail, E E Bodor, Some remarks about capillary condensation and
646 pore structure analysis, Journal of Colloid and Interface Science, vol. 25, n° 3, 1967, pp 883-
647 892.

648 [16]: V Baroghel Bouny, Water vapour sorption experiments on hardened cement based
649 materials, Part I: Essential tool for analysis of hygral behaviour and its relation to pore
650 structure. Cement and Concrete Research, vol. 37, n°3, 2007, pp 414-437.

651 [17] : V Baroghel Bouny, Caractérisation des pâtes de ciment et des bétons : Méthodes,
652 analyse, interprétations, PhD Thesis, Ecole Nationale des Ponts et Chaussées, 1994.

653 [18] : T Ishida, K Maekawa, T Kishi, Enhanced modeling of moisture equilibrium and
654 transport in cementitious materials under arbitrary temperature and relative humidity history,
655 Cement and Concrete Research, vol. 37, 2007, pp 565-578.

656 [19] : S Poyet, Experimental investigation of the effect of temperature on the first desorption
657 isotherm of concrete, Cement and Concrete Research, vol. 39, n°11, 2009, pp 1052-1059.

658 [20] : R M Espinosa, L Franke, Influence of the age and drying process on pore structure and
659 sorption isotherms of hardened cement paste, Cement and Concrete Research, vol. 36, n°10,
660 2006, pp 1969-1984.

661 [21] : P C Philippi, H A Souza, Modelling moisture distribution and isothermal transfer in a
662 heterogeneous porous material, International Journal of multiphase flow, vol. 21, n°4, 1995,
663 pp 667-691.

664 [22]: B Bary, A polydispersed particle system representation of the porosity for non saturated
665 cementitious materials, Cement and Concrete Research, vol. 36, n°11, 2006, pp 2061-2073.

666 [23]: J Carmeliet, F Descamps, G Houvenaghel, A multiscale network model for simulating
667 moisture transfer properties of porous media, Transport in Porous Media, vol.35, n°1, 1999,
668 pp 67-88.

669 [24]: M Hilpert, R Glantz, T Miller Cass, Calibration of pore-network model by a pore-
670 morphological analysis, Transport in porous media, vol.51, n°3, 2003, pp 267-285.

671 [25] : B Ahrenholz, J Tölke, P Lehmann, A Peters, A Kaestner, M Krafczyk, W Durner,
672 Prediction of capillary hysteresis in a porous material using lattice-Boltzmann methods and
673 comparison to experimental data and a morphological pore network model, Advances in
674 water resources, vol. 31, n°9, 2008, pp 1151-1173.

675 [26]: D Quenard, H Sallee, Water vapour adsorption and transfer in cement based materials: a
676 network simulation, Materials and Structure, vol. 25, n°153, 1992, pp 515-522.

677 [27] : R M Espinosa, L Franke, Ink-bottle pore method: prediction of hygroscopic water
678 content in hardened cement paste at variable climatic conditions, Cement and Concrete
679 Research, vol. 36, n°10, 2006, pp 1954-1968.

680 [28] : K Maekawa, T Ishida, T Kishi, Multi-scale modeling of structural concrete, 2009

681 [29] : N Hyvert, Application de l'approche probabiliste à la durabilité des produits
682 préfabriqués en béton, PhD Thesis, Université de Toulouse, 2009.

683 [30]: G Camps, Etude des interactions chemo-mécaniques pour la simulation du cycle de vie
684 d'un élément de stockage en béton, PhD Thesis, Université de Toulouse, 2009

685 [31] : V Waller, Relations entre composition des bétons, exothermie en cours de prise et
686 résistance en compression. PhD thesis, Ecole Nationale des Ponts et Chaussées. 1999

687 [32]: T C Powers, T L Brownyard, Studies of the physical properties of hardened Portland
688 cement paste, Research bulletin 22, Portland Cement Association, Chicago, IL (1948) reprint
689 from Journal of American Concrete Institute in Proceedings 43 (1947).

690 [33] : F Adenot, Durabilité du béton : caractérisation et modélisation des processus physiques
691 et chimiques de dégradation du ciment. PhD Thesis, Université d'Orléans.1992

692 [34]: B Bary, A Sellier, Coupled moisture-carbon dioxide-calcium transfer model for
693 carbonation of concrete, Cement and Concrete Research, vol. 34, 2004, pp 1859-1872.

694 [35] : I G Richardson, The nature of C-S-H in hardened cement, Cement and Concrete
695 Research, vol.29,n°8, 1999, pp 1131-1147

696 [36] : M D Nguyen, Modélisation des couplages entre hydratation et dessiccation des
697 matériaux cimentaires à l'issue du décoffrage, Etude de la dégradation des propriétés de
698 transfert, PhD Thesis, Ecole Nationale des Ponts et Chaussées, 2009.

699 [37]: HFW Taylor, Cement Chemistry, Academic Press, London 1990

700 [38]: S Mindess, J F Young, Darwin D, Concrete, 2nd Edition, Prentice Hall, Englewood
701 Cliffs, NJ, 2002.

702 [39]: F Brue, Rôles de la température et de la composition sur le couplage thermo-hydro-
703 mécanique des bétons, PhD Thesis, Ecole Centrale de Lille.

704 [40] : H Loosveldt, Z Lafhaj, F Skoczylas, Experimental study of gas and liquid permeability
705 of a mortar, Cement and concrete research, Vol. 32, n°9, 2002, p 1357-1363.

706 [41] : AFPC-AFREM, Durabilité des bétons, Compte rendu des journées techniques
707 « Méthodes recommandées pour la mesure des grandeurs associées à la durabilité »,
708 Toulouse, 1997

709 [42]: V Baroghel Bouny, Water vapour sorption experiments on hardened cement based
710 materials, Part II: Essential tool for assessment of transport properties and for durability
711 prediction. Cement and Concrete Research, vol. 37, n°3, 2007, pp 438-454.

712 [43]: R.M.E Valckenborg, L. Pel, K. Hazrati, K. Kopinga, J. Marchand, Pore water
713 distribution in mortar during drying as determined by NMR. Materials and Structures, vol.34,
714 n°10, 2001, pp 599-604.

715 [44]: A Nonat, The structure and stoichiometry of C-S-H. Cement and Concrete
716 Research, vol.34, n°9, 2004, pp 1521-1528.

717 [45]: HFW Taylor, Proposed structure for calcium silicate hydrate gel, Journal of the
718 American Ceramic Society, vol.69, 1986, pp 464-467

719 [46]: J P Monlouis Bonnaire, Modélisation numérique des transferts couplés air-eau-sel dans
720 les matériaux cimentaires et les terres cuites, PhD Thesis, Université Paul Sabatier, 2003

721 [47]: S Brunauer, P H Emmett, E J Teller, Adsorption of gases in multimolecular layers,
722 Journal of the American Chemical Society, 60, 1938, pp 309.

723 [48]: Y Xi, Z P Bazant, H M Jennings, Moisture diffusion in cementitious materials,
724 Advanced cement based materials, vol.1, n°6, 1994, pp 248-257.

725 [49]: www.scilab.org

726 [50]: A S El Dieb, R D Hooton, Evaluation of the Katz Thompson model for estimating the
727 water permeability of cement based materials from mercury intrusion porosimetry data,
728 Cement and Concrete Research, vol. 24, n° 3, 1994, pp 443-455.

729 [51]: L Cui, J H Cahyadi, Permeability and pore structure of OPC paste, Cement and
730 Concrete Research, vol. 31, n°2, 2001, pp 277-282.

731 [52]: M R Nokken, R D Hooton, Using pore parameters to estimate permeability or
732 conductivity of concrete, Materials and Structure, vol. 41, n°1, 2008 pp 1-16

733 [53]: J J Zheng, X Z Zhou, Analytical method for prediction of water permeability of cement
734 paste, ACI materials journal, Vol.105, n°2, 2008, pp 200-206.

735 [54]: F Dullien, Porous Media Fluid Transport and Pore Structure, New York Academic
736 Press, 1979

737 [55] : J P Ollivier, J M Torrenti, La structure poreuse des bétons et les propriétés de transfert,
738 in La durabilité des bétons sous la direction de Ollivier J.P, Vichot A, 2008

739 [56]: S C Carniglia, Construction of the tortuosity factor from porosimetry, Journal of
740 catalysis, vol. 102, n° 2, 1986, pp 401-418.

741 [57] : M Matyka, A Khalili, Z Koza, Tortuosity-porosity relation in the porous media flow,
742 Physical Review E, vol. 78, n°2, 2008, pp 1-8

743 [58]: J Comiti, M Renaud, A new model for determining mean structure parameters of fixed
744 beds from pressure drops measurements: application to beds packed with parallelepipedal
745 particles, Chemical Engineering Sciences, vol.44, n°7, 1989, pp 1539-1545.

746

747

748 .

749